Laser-based diagnostics and scalar imaging in high compressibility shear layers

by

T. Rossmann[(1)], M. G. Mungal[(2)], R. K. Hanson[(3)]

High Temperature Gasdynamics Laboratory

Mechanical Engineering Department

Stanford University, Stanford, California 94305

[(1)] Email: rossmann@advancedprojects.com

[(2)] Email: mungal@stanford.edu

[(3)] Email: hanson@me.stanford.edu

ABSTRACT

Quantitative scalar imaging of high compressibility mixing layers is performed in a shock tunnel-driven hypersonic mixing layer facility. A high sensitivity Planar Laser-Induced Fluorescence (PLIF) scheme using nitric oxide as the seeded species along with appropriate mixing layer conditions is developed to instantaneously measure local mixture fraction of a conserved scalar in a non-isothermal environment. Signal dependencies on local temperature, laser fluence, and quenching environment are calculated and optimized to ensure quantitative PLIF images of mixture fraction. These images provide detailed information about the behavior of large-scale structures and turbulent dynamics in compressible mixing layers. For the imaged mixing layer at $M_c = 2.64$, streamwise structures, inclined in the flow direction from the side view, are seen to dominate the scalar field of the shear layer and the mixing dynamics. Side, plan, and end views show strong instantaneous transverse gradients in mixture fraction, suggesting that gradient transport models for scalar mixing are likely appropriate at high compressibilities where the structure size is smaller and reduced pressure communication inhibits large-scale mixing.

[1] Current Address:
Advanced Projects Research Inc. (APRI)
1925 McKinley Ave., Suite B.
La Verne, CA 91750

1. INTRODUCTION

Since the discovery of large-scale structures in mixing layers by Brown and Roshko (1974), many investigators have sought to describe the effects of compressibility on the shear layer in terms of the shape and extent of these large-scale structures as well as the effect of these structures on the instantaneous mixing profiles. The Schlieren images of Papamoschou and Roshko (1988) demonstrated the presence of well-defined large-scale structures at low compressibility conditions (M_c <0.7). Clemens and Mungal (1995) clearly characterized the effects of compressibility on structures up to $M_c = 0.8$. They showed that well-defined spanwise-oriented, Brown-Roshko type rollers exist below M_c of 0.3. Above this, the structures transition into less organized, diffuse elements. Above $M_c \sim 0.5$, oblique instability modes begin to skew the spanwise rollers so that strong three-dimensionality is present in the layer. Plan view images of both passive scalars and product formation methods confirmed this decrease in spanwise uniformity and the increased obliquity.

The dynamics of the shear layer and insights into how the large-scale structures behave and enhance the local mixing are of great importance for many high-speed mixing applications. The reduction in growth rate of shear layers with increasing compressibility, in addition to the behavior of large-scale structures, has been well documented. Samimy *et al.* (1990) studied a fairly high compressibility condition ($M_c = 0.86$) using static pressure correlations to determine that structure lengths decreased at high compressibilities, and found that this evidenced increasing three-dimensionality. Naughton *et al.* (1997) showed that reduced pressure communication across the shear layers inhibited vortex roll-up and pairing events, thereby causing weak elongated streamwise structures to be preferred at high compressibilities (above convective Mach number of one). Morkovin (1992) found that streamwise vortical structures are not subject to communication problems like spanwise rollers as they primarily interact in the spanwise direction, rather than across the layer. Thus, these structures continue to enlarge and extract energy from the mean flow and entrain fluid into the layer. Rossmann *et al.* (2002) showed that streamwise structures dominate the flow topology above $M_c = 1$, engulfing free stream fluid into the shear layer but with slow internal mixing.

For instantaneous measurements of scalar mixedness and large-scale structure, two-dimensional imaging is a most useful tool. Large-scale structure interactions as well as their internal scalar fields can be examined in a spatially resolved sense. Planar Laser-Induced Fluorescence (PLIF) allows for high spatial resolution, instantaneous 2-D imaging of local thermodynamic conditions in fluid flows (Hanson *et al*, 1990) if the spectroscopy of the excited molecule is well known. There have been numerous scalar measurements for mixing layers at various lower compressibilities. Clemens and Mungal (1995), using PLIF of a seeded tracer species, found that the scalar transverse fluctuations decreased with increasing compressibility. Also, they noted that a marching PDF was seen for both cases ($M_c = 0.28$ and 0.62), with the peaks of mixed fluid composition about 20% wider for the low compressibility case. Dutton *et al.* (1990), using planar Mie scattering, also found marching PDFs and a slight increase in mixing efficiency for his conditions of $M_c = 0.3$ and 0.77. However, each of these studies occurred at low shear rates where viscous heating is negligible and temperature acts as a conserved scalar in a non-isothermal flow field. Thus, the instantaneous temperature and mixture fraction variations are the same and a temperature correction can be derived from the images.

When imaging large-scale structures in supersonic mixing layers, it is desirable to have an optical diagnostic whose signal is proportional only to the local mole fraction of one of the free streams, independent of both local pressure and temperature. This becomes even more important in high compressibility shear layers where temperature no longer acts as a conserved scalar and thus cannot be corrected for in the post-processing of fluorescence images using a mixture fraction correlation. In order to create such a diagnostic, the issues of tracer selection and seeding, transition selection, saturation, quenching environment, and other potential systematic errors must be examined. This paper will describe the design and application of a NO PLIF measurement technique for examining the local mixture fraction field in a high compressibility shear layer.

(a)

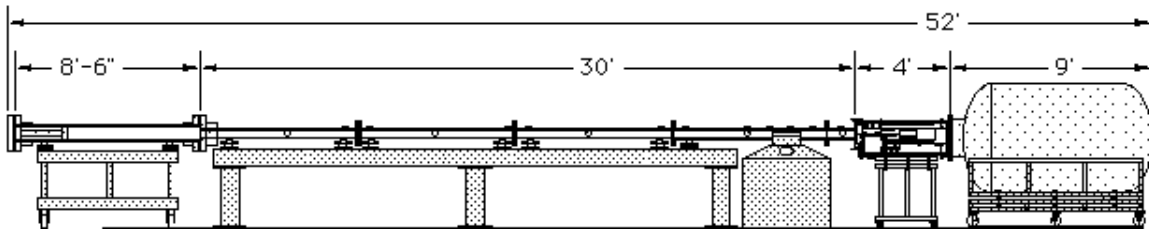

(b)

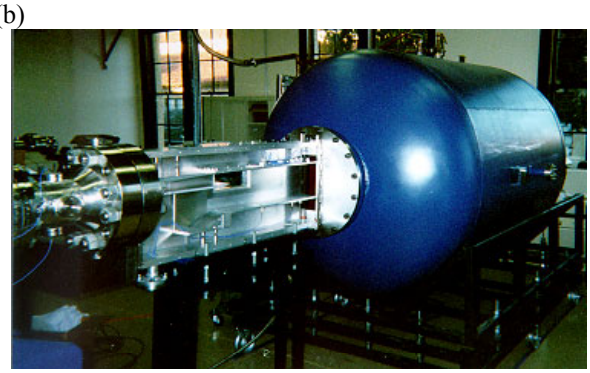

(c)

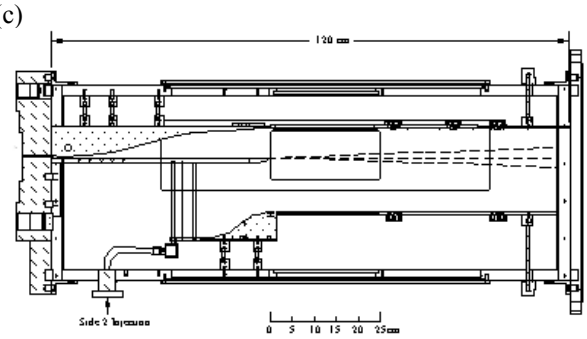

Fig. 1 (a) Schematic of Stanford Shock Tunnel. (b) Image showing hypersonic mixing facility between shock tunnel and dump tank. (c) Schematic of mixing facility showing imaging locations, supersonic and subsonic nozzles as well as variable angle inner walls.

2. EXPERIMENTAL FACILITY AND METHODS

2.1 Shock Tunnel

This study was conducted using the Stanford Shock Tunnel coupled to a specialized hypersonic mixing layer facility whose details of have been previously described in greater detail (Rossmann *et al.,* 1999). The shock tunnel (Fig. 1a) consists of a 2.6m long driver section (18 cm internal diameter) and a 9.1m long driven section (11.4 cm internal diameter). It is fired in a double diaphragm mode to give adequate flow set up time to secondary flow devices. A 10 cm x 5 mm slot is cut into the endwall to form the throat for the various nozzles that are coupled to the shock tube. The tunnel is designed to handle pressures up to 150 atm, which allows for cross flows in the mixing layer facility of up to M = 6 at test section pressures of at least 0.1 atm.

Shock speed information and laser sync pulses are obtained from five PCB 113A21 piezoelectric transducers mounted at 30.5 cm intervals. Pressure measurements are also made inside the mixing layer facility to quantify the streamwise pressure gradients caused by high speed mixing layers. The upper and lower walls of the test section are then angled to relieve these pressure gradients.

2.2 Mixing Layer Facility

The mixing layer facility (Fig. 1b and c) houses a two-dimensional supersonic nozzle block (which draws from the shock tunnel), a splitter plate, a subsonic nozzle, and a low speed manifold used to inject the subsonic portion of the mixing layer. This subsonic portion is provided by a small blow down tank, which is activated 200-300 msec before the firing of the shock tube to allow adequate time for the low speed flow to develop. The exit of the mixing facility is joined to a 3 m^3 dump tank, which is used to maintain a constant test section pressure during the test time. Various nozzle blocks are used to create fast side Mach numbers of 3.3, 3.9, and 5.2. With these nozzles, variable diaphragm pressure ratios, and easily variable low-speed side mixtures, the convective Mach number achieved in the test section is continuously variable from M_c = 0.8 to 2.9.

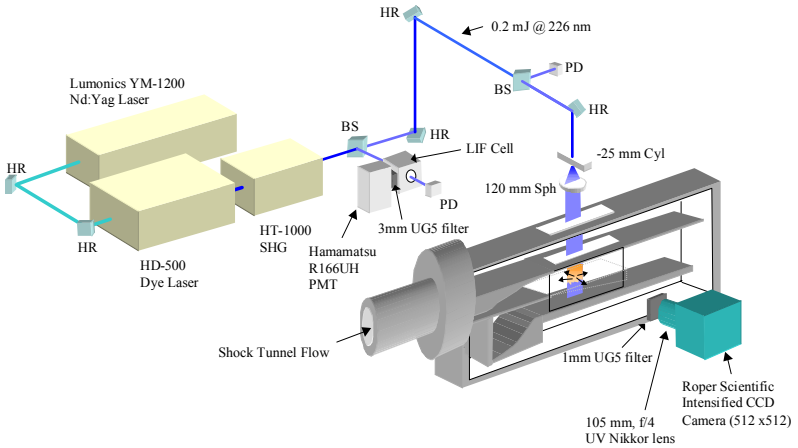

Fig. 2 NO PLIF imaging setup using for this paper. HR = High reflector, optimized for input wavelength and 45° reflection; BS = Beam splitter, fused silica glass slides giving 8% reflection; PD = Photodiode, fitted with a phosphor mask to make it sensitive to UV radiation; PMT = Photomultiplier Tube; Cyl = Cylindrical lens for beam expansion; Sph = Spherical lens for laser sheet collimation and focusing.

2.3 NO PLIF Imaging System

Since nitric oxide is not a broad band absorber, but has discrete absorption lines in the UV, the excitation scheme for NO PLIF requires a tunable laser source for this type of diagnostic. The diagnostic setup is shown in Fig. 2. The frequency tripled output of a Nd:YAG laser pumps a dye laser with Coumarin 2 dye, lasing at 452 nm and tuned by an intracavity grating. The dye laser output is then frequency doubled in BBO to 226 nm and tuned to the $A^2\Sigma^+ \leftarrow X^2\Pi^{1/2}$ (0,0), $Q_1 + P_{21}$ (18.5) transition at 225.857 nm. The laser has a temporal pulse width of 6.8 nsec, a spectral width of 0.5 cm^{-1}, and an energy of 0.1 mJ at the imaging location. The beam is formed into a 140 μm x 45 mm sheet using a cylindrical and spherical lens combination (Fig. 2). The sheet is directed into the test section either from above (for side view imaging) or from the side (for plan and end view imaging). Sheet thickness and size do not vary significantly between these orientations. Shot-to-shot laser power fluctuations are monitored by a 1mm photodiode with a phosphor mask.

The NO fluorescence is captured by an intensified CCD camera (512 x 512 array with 20 μm pixels), coupled to a UV Nikkor lens (105 mm, f/4). The exposure of the CCD array is gated to 250 nsec to capture the NO fluorescence (characteristic time of ~ 140 nsec at the shock tunnel conditions) plus the time associated with the temporal jitter of the timing electronics. A 1 mm Schott UG-5 filter is placed before the camera to block any elastic scatter, but allows fluorescence from the (0,1) to (0,7) bands of NO into the camera. The wavelength of the laser is calibrated to the NO spectrum by the use of an LIF cell. Part of the beam is diverted into a cell fitted with opposed fused silica windows, and a 50 mm f/2 lens, mounted perpendicularly to the beam, focuses the LIF onto a Hammamatsu R166UH photomultiplier tube. A gate delay generator is used to integrate the signal for 300 nsec after the laser pulse.

The raw fluorescence images are corrected for camera dark background, non-uniform spatial response of the camera/collection optics, and spatial distribution of the laser energy. Instantaneous sheet corrections are performed in the side view images only, as the plan and end views do not possess uniformly seeded regions spanning the laser sheet. For those views, 8 frames are averaged, and each instantaneous image is corrected with the average laser profile. The processed images are binned 3x3 to improve signal to noise ratio, leading to a resolution in the side and plan views of approximately 140 x 280 x 280 μm. The peak signal to noise ratio for the side and plan view NO images is 12, for the end views, SNR = 20. Because the end view images are taken at an angle of 30 degrees to the flow axis, these raw images are corrected to make the images appear rectilinear. Because of this correction and the different field of view from the side/plan views, the resolution for the end views is 140 x 170 x 170 μm.

3. NO PLIF DIAGNOSTICS ISSUES

For a temperature insensitive diagnostic, careful selection of the excitation transition and quenching environment is required. The selection of the pumping transition (and thus the variation of its Boltzmann fraction with temperature) depends on the temperature range of interest for the experiment. For the $M_c = 2.64$ condition examined in this study, the free stream static temperatures are 390 K and 289 K for the fast and slow streams respectively. Thus, the mixed states are expected to range in temperature from 300 K up to a hot zone in the center of the mixing layer where the fast stream has been decelerated and the slow stream accelerated. In the analysis of this diagnostic, little *a priori* knowledge of this aerodynamic heating is documented, as the heating depends on the relative entrainment ratios of the two streams and the local convection velocity of structures.

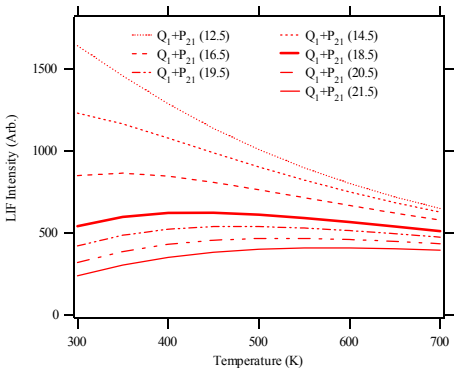

Fig. 3 Variation of LIF signal for NO tracer species pumped by a resonant broad laser pulse at different A←X, Q_1+P_{21} rotational transitions as computed using the 4-level LIF model from Appendix C. Simulations are performed at 0.1 atm with 2300 ppm NO in 95% Argon, 3.9% N_2, and 0.8% O_2.

Assuming an upper boundary of 700 K on the temperature range of the experiment, the solution to a 5-level model fluorescence equation as a function of temperature will lead to the choice of the most temperature-insensitive pumping transition. Shown in Fig. 3 are the relative fluorescence signals from some $Q_1 + P_{21}$ transitions (which have the highest Einstein A coefficient in the A←X band). Immediately apparent from this plot is that the LIF signal will decrease with increasing rotational quantum number due to decreasing Boltzmann populations. Also, there are regions of temperature for each transition shown where the curves are nearly flat, which permits LIF signals that are insensitive to temperature in those ranges. As a check of the simulation produced by this study, a similar examination of the $J'' = 18.5$ and surrounding rotational transitions was performed using the NO spectra simulation tool of Bessler and Sick (Private communication, 2001). These results are shown in Fig. 4a, and the overall change in the absorption feature as a function of temperature well matches the previous results as well as NO LIF data taken from a static cell (Fig. 4b).

Since these supersonic experiments take place at low pressures, the quenching rates are nearly equal to the spontaneous emission rates. The signal is therefore not quench dominated as it is at standard conditions. A full dynamic simulation of the fluorescence is required to ensure that the signal remains unsaturated and linear in the local mixture fraction of the seeded tracer species. The temporal dynamics of the fluorescence process at lower pressure LIF experiments introduces the potential for saturation of the electronic transition and the significant perturbation of the ground state rotational distribution, as rotational energy redistribution rates (RET) are slow. A 5-level LIF model was again used to examine saturation effects at the thermodynamic conditions of the mixing layer. Saturation effects become important (> 10%) above a spectral power of 1 MW/cm^2 cm^{-1} in good agreement with a LIF modeling analysis done by Lee *et al* (1993). Consequently, the average laser fluence in this experiment is kept below 0.5 MW/cm^2 cm^{-1} to ensure that saturation effects do not play a role.

Another important consideration for making accurate measurements of local high-speed fluid mole fraction is the change in the quenching environment as the seeded stream mixes with the unseeded, lower speed stream. If the packet of mixed fluid has a different quenching environment than the upper free stream, the fluorescence quantum yield will not be the same locally. Thus, the LIF signal will not scale linearly with the local mole fraction of high-speed fluid, as can be shown by examining the variation in Eqn. 1 across the mixing layer.

$$S_f \propto \chi_H \phi(P,T,\chi_i) \quad where \quad \phi \cong \frac{A_{21}}{A_{21} + \sum_{all\ species} \chi_i \frac{P}{kT} \sigma_i(T) \langle v_i(T) \rangle} \qquad \text{Eqn. 1}$$

However, if the lower speed stream mixture can be constructed such that the product of $\Sigma\chi_i\,\sigma_i\,\langle v_i\rangle$ is equal to that of the high stream, then the quenching environment will be the same in all the mixed states. This will be termed an "iso-quenching" environment. The effect of using an iso-quenching environment is shown in Fig. 5. Using the quenching cross sections (σ_i) from McDermid and Laudenslager (1982), the quenching rate in the mixture 98.8% argon, 1.2% O_2 exactly balances the quenching in the supersonic free stream (95% argon, 3.97% N_2, 0.8% O_2, 0.23% NO). The relative error in the mole fraction measurement increases as the lower speed mole fraction (χ_L) increases in the mixed states for non-matched quenching environments. The mixture fraction error due to mixing using an iso-quenching environment is reduced to 0.3% at the minimum detectable level over the temperature range from 300 to 700K. Thus, it is clear that the potential errors associated with the mixing of the two streams to different local mole fractions and temperatures are minimized by the use of an iso-quenching mixing environment.

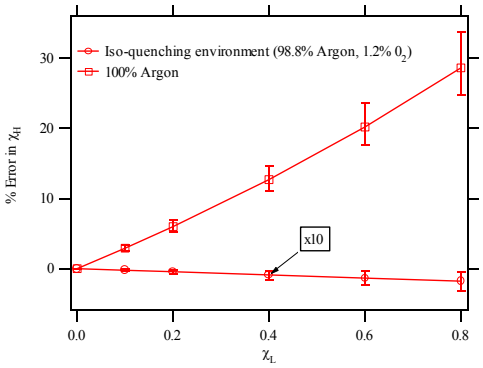

Fig. 5 Computation of the relative error in determining the mixture fraction of high-speed side fluid (χ_H) in the shear layer as it mixes with low speed fluid (χ_L) when not using an iso-quenching environment. Quenching cross-sections are taken from McDermid and Laudenslager (1982), and the simulations are performed at 0.1 atm with 2300 ppm NO in 95% Argon, 3.9% N_2, and 0.8% O_2. The error bars denote the range of errors for 300 – 700 K.

4. RESULTS AND DISCUSSION

4.1 Test Conditions

For these measurements, NO is produced in the shock tunnel at initial conditions of 3650 K and 31 atm. A mixture of 95% argon and 5% dry air is used as the test gas and shocked by a $M_s = 4.10$ incident wave. The test time for this shock condition is 1.95 msec and nozzle start time is 450 μsec. Consequently, the layer is allowed to develop for 1.5msec before PLIF images are taken. The maximum laser fluence for these experiments is 0.45 MW/cm^2 cm^{-1} which is below the saturation level for these conditions. The test section upper wall is set to 0 degrees while the lower wall is set to -0.5 degrees) to minimize the streamwise pressure gradient. The mixing layer variables for this condition are shown in Table 1.

4.2 Side View Images

Fig. 6 shows four instantaneous images with transverse and streamwise cuts displayed. Nitric oxide was seeded in the upper high-speed stream by its creation in the stagnation conditions of the shock tunnel and flow is from left to right. The field of view extends from 16 to 20.3 cm downstream of the splitter plate and from –2.7 cm < y < 2.0 cm. These side view images are taken on the centerline of the test section (z = 0). The peak SNR for these images is 12. The field of view encompasses approximately 3 mixing layer thicknesses in both height and width. Very few instances of true Brown-

Table 1 Mixing layer conditions for the $M_c = 2.64$ case

$M_{c\,avg}$	2.64	$M_{exit\,1}$	4.87
M_{c1}, M_{c2}	2.64, 2.64	M_1, M_2	5.12, 0.30
$P_{test\,section}$ [atm]	0.10	s	1.369
Gas_1	95% Argon, 5% Air	r	0.05
Gas_2	98.8% Argon, 1.2% O_2	$(\delta)_{x\,=\,18\,cm}$ [cm]	1.2
T_1, T_2 [K]	390, 289	$(Re_\delta)_{x\,=\,18\,cm\,1,2}$	9.6 x 10^4, 1.6 x 10^5
V_1, V_2 [m/sec]	1880, 94	$(Re_x)_{avg}$	1.88 x 10^6
$\dot{m}_1$, $\dot{m}_2$	0.69, 0.10 (kg/sec)	$(\delta/\Delta V)_{x\,=\,18\,cm}$ [μs]	6.7

Roshko type large-scale rollers are seen in these images. The layer interface on the high-speed side appears very ragged and the layer thickness does not vary greatly with downstream distance in the field of view, suggesting very few streamwise correlated structures, common at low compressibilities. There are also very few regions of pure low-speed fluid near the high-speed stream interface, in contrast to the lower M_c results. Engulfing entrainment motions do not appear to be as prevalent at this compressibility condition. The layer also appears internally well mixed, with a reasonably smooth variation of mixture fraction in the cross-stream direction for most structures.

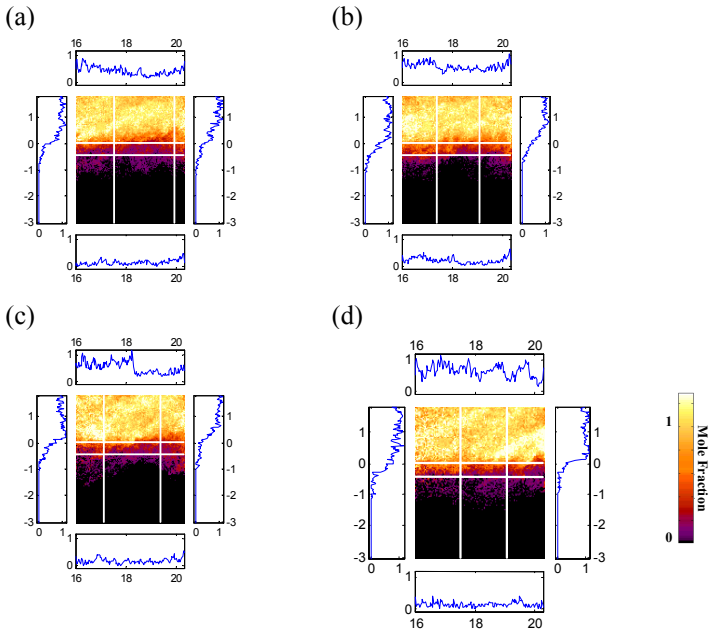

Fig. 6 Instantaneous passive scalar side view images at M_c = 2.64 with fast-side seeding. Flow is left to right with the high-speed stream on top. The imaged region is Δx = 4.3 cm and Δy = 4.7 cm and centered 18 cm downstream of the splitter tip and aligned with the centerline of the test section. The images are uncorrelated in time. Plotted alongside each image is the high-speed mixture fraction versus distance (in cm) along the streamwise and cross-stream lines indicated. Color map interpretation of mixture fraction is shown to the right of image d.

The layer thickness in this set of images varies widely. This type of variation was witnessed in the end views of lower compressibility conditions, where large structures are separated by thin braid regions in the streamwise direction. Thus, end view images can capture either large structures (where the mixing layer appears at its full average thickness) or the braid regions (where the layer appears much thinner than the average thickness). The same type of effect is seen here in the side view images of Fig. 6. Consequently, large-scale streamwise structures with some spanwise periodicity must exist in order to provide side view images where the layer thickness varies greatly. In Fig. 6, each graph of local mixture fraction flanking the images corresponds to the closest parallel line through the layer (which denotes the position of the cross section). All graph axes are in units of cm downstream (in the case of the streamwise cuts) or cm from the origin set at the 50% level of the average mixture fraction profile (in the case of the cross-stream cuts). The upper streamwise cuts are taken at the 50% level of the average mixture fraction profile, while the lower streamwise cuts are taken at the 20% level.

In all of the streamwise cuts, very few streamwise ramps are in evidence, suggesting that there are few significant spanwise-oriented structures like those seen at low compressibilities. Some very slight streamwise ramps are present in images (b) and (c) and are perhaps caused by some spanwise coherent structures of limited extent. The cross-stream cuts show almost uniformly that the structures in the mixing layer are strongly ramped in the cross-stream direction. These ramps suggest that the dominant entrainment motions are streamwise, rather than spanwise.

4.3 Plan View Images

Five instantaneous plan view images for the M_c = 2.64 condition are shown in Fig. 7. The field of view extends from 16 to 19.7 cm downstream from the splitter tip and from z = -1.9 cm to 1.9 cm, and the flow is from left to right. These images are taken at the y = 0 level, through the 50% mixture fraction level of the average mixing layer profile. Images are corrected for laser sheet non-uniformity using the streamwise intensity distribution of the average image. The peak SNR for these images is 15 owing to the slightly smaller field of view as compared to the side view images.

These images reveal a set of strong streamwise structures (about one per image), which are oriented nearly parallel to the flow direction. The streamwise structures appear to be at a nearly uniform value of mixture fraction along their length. Outside of the streamwise structures, the mixture fraction field appears generally to be ramped in the spanwise direction and relatively constant in the streamwise direction. The few streamwise cross-sections, which exhibit some ramps, are mostly correlated with the edges of these streamwise structures existing within the cut.

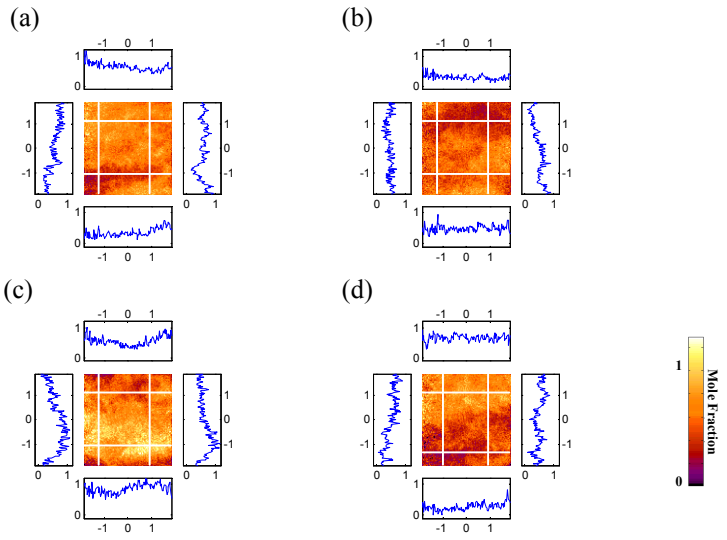

Fig. 7 Instantaneous passive scalar plan view images at M_c = 2.64 with fast-side seeding. Flow is left to right. The imaged region is Δx = 3.7 cm and Δz = 3.8 cm and centered 18 cm downstream of the splitter tip and aligned with the centerline of the test section. The images are uncorrelated in time.

The layer also shows significant spanwise ramps in mixture fraction profile in all the images. These ramps are consistent with spanwise-localized streamwise structures engulfing and mixing low-speed fluid in streamwise oriented streamtubes. Therefore, as these structures continue to propagate downstream, the stepped spanwise profiles caused by the gross entrainment behavior of the streamwise structures will be smoothed out into spanwise ramps. It is interesting to note that for every spanwise cross section that exhibits these ramps, there is another that does not. This reinforces the idea that these streamwise structures, while longer than one to two average mixing layer thicknesses, are still bounded in their downstream extent, and the effect of their mixing is still localized in the streamwise direction.

4.4 End View Images

Five instantaneous end view images for the M_c = 2.64 condition are shown in Fig. 8. The field of view extends from z = -2.6 cm to 2.6 cm and from y = -1.8 cm to 0.9 cm, and the flow is into the page. These images are taken at x = 18 cm downstream of the splitter tip. The images demonstrate the varied states of the streamwise structures as they propagate downstream. Image (d) shows two streamwise structures that have likely just entrained large amounts of low-speed fluid and transported it in an engulfing motion to the high-speed side of the layer. Image (b) shows the same characteristics, but the streamwise structures imaged here are more mixed. This trend of structures appearing more mixed as they propagate downstream is reinforced by images (a), (c), and (d). Though each image is from a separate firing of the shock tunnel and not correlated with the others, the images do display streamwise structures at varying degrees of internal mixedness, which is consistent with the engulfing entrainment and subsequent mixing model. Structures which are smaller than the layer thickness appear to be better mixed. Larger structures tend to have strong vertical mixture gradients across them, supporting the idea that these larger structures engulf low-speed fluid in a sweeping motion and transport it across the layer before it has a chance to mix. This behavior also is consistent with the "sonic eddy" concept (Breidenthal, 1992), whereby the largest structures must have an eddy rollover timescale which is shorter than the local acoustic time-scale causing reduced turbulent mixing internal to the structure.

Transverse and spanwise cross sections through the end view images are also shown in Fig. 8. The transverse cuts demonstrate streamwise structures in various stages of internal mixedness. The cuts from images (a) and (d) display sharp drop-offs in cross-stream scalar profiles consistent with the engulfing streamwise structures that have yet to mix internally. Cross-stream sections from the other images show a layer with well-defined cross-stream ramps, consistent with the results from the side view images. The upper spanwise cuts are taken at the 50% level of the average mixture fraction profile, while the lower spanwise cuts are taken at the 20% level. Both spanwise ramps and

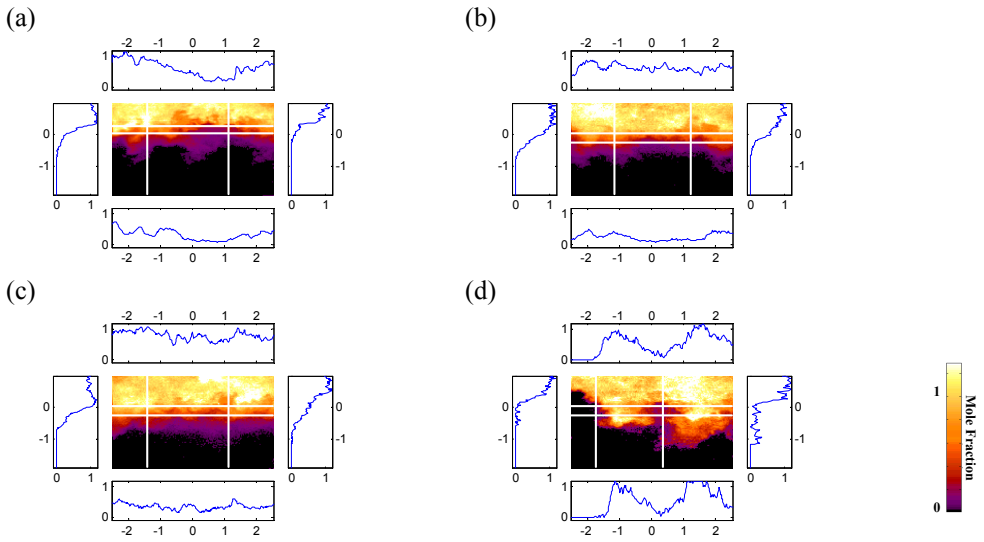

Fig. 8 Instantaneous passive scalar plan view images at M_c = 2.64 with fast-side seeding. Flow is into the page with the high-speed stream on top. The imaged region is Δy = 2.7 cm and Δz = 5.2 cm and centered 18 cm downstream of the splitter tip. The images are uncorrelated in time. Plotted alongside each image is the high-speed mixture fraction versus distance along the streamwise and spanwise lines indicated.

spanwise uniform cross-sections are evident in the spanwise mixture fraction profiles, which is similar to the plan view images. Furthermore, the spanwise-localized structures that cause the spanwise ramps and shear layer thickness intermittency in the side view images are now clearly seen.

4.5 Average Images

Shown in Fig. 9 are the frame-averaged images for all three imaging planes. Eight instantaneous, corrected images are averaged, so the concentration profiles are likely not completely converged, especially in directions where the intermittency is high. The transverse profiles shown in both the side and end view images are similar to most compressible mixing layer cross-stream profiles. However, the instantaneous profiles of Fig 6 are very similar to the average profile, suggesting that the instantaneous large-scale structures are locally well mixed internally. The averaged profiles in the spanwise direction from the plan and end view images are fairly flat; however, high levels of streamwise structure intermittency causes these averages not be quite converged for this small sample set. Conversely, the average streamwise profiles are much more uniform because the streamwise structures have large aspect ratios (seen in the instantaneous plan view images) and

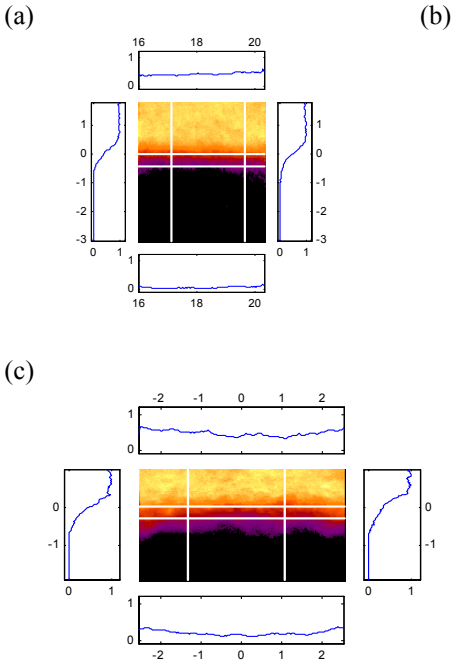

Fig. 9 Profile of average images: (a) side, (b) plan, (c) end. Each average is an 8 frame average of instantaneous corrected images. Colormap is the same as all previous images. Transverse profiles are taken at y = 0.5 and y = 0.2. Plan view (b) is taken at y = 0.5.

do have high levels of intermittency in the streamwise direction.

5. CONCLUSIONS

Variations on established nitric oxide PLIF diagnostics were developed and employed to quantitatively image mole fraction in a non-isothermal, low pressure, mixing flowfield. Careful selection and modeling of the electronic transition, quenching environment, and LIF signal allowed for a straightforward diagnostic which yielded acceptable SNR and small mixture fraction uncertainty over a wide temperature range. Utilization of this diagnostic enabled the close examination of the instantaneous mixture fraction field of a mixing layer at very high compressibility. The high speeds in this flowfield lead to large uncertainties in the instantaneous local temperature field, requiring an optical diagnostic which is insensitive to local temperature.

For the imaged mixing layer at $M_c = 2.64$, streamwise structures, inclined in the flow direction from the side view, were seen to dominate the scalar field of the shear layer. The streamwise structures appeared to engage in entrainment motions, engulfing large amounts of free-stream fluid and transporting it across the shear layer before the structures were internally mixed. The structures showed strong instantaneous cross-stream ramps, suggesting that gradient transport models for scalar mixing are likely appropriate at high compressibilities where the structure size is smaller and reduced pressure communication inhibits large-scale mixing. Strong spanwise ramps were apparent in large-scale structures which had yet to mix internally, further suggesting that the streamwise structures had some associated spanwise motions. The similarity of the mean transverse profile to the instantaneous transverse profile suggests that gradient diffusion models for scalar transport and mixing may be more successful at higher convective Mach number conditions than large-scale structure based models which appear to be more suitable for lower convective Mach number conditions.

6. REFERENCES

Breidenthal, R.E. (1992) "Sonic Eddy: A Model for Compressible Turbulence," *AIAA Journal*, Vol. 30, No. 1, pp. 101-104.

Brown, G.L. and Roshko, A. (1974) "On Density Effects and Large Structures in Turbulent Mixing Layers," *J. Fluid Mech.,* Vol. 64, pp. 775-816.

Clemens, N.T. and Mungal, M.G. (1995) "Large-scale Structure and Entrainment in the Supersonic Mixing Layer," *J. Fluid Mech.*, Vol. 284, pp. 171-216.

Dutton, J.C., Burr, R.F., Goebel, S.G., and Messersmith, N.L. (1990) "Compressibility and Mixing in Turbulent Free Shear Layers," 12th Symposium on Turbulence, Rolla, MO.

Hanson, R.K., Seitzman, J.M., and Paul, P.H. (1990) "Planar Laser-Fluorescence Imaging of Combustion Gases," *Appl. Phys. B*, Vol. 50, pp. 441-454.

Lee, M.P., McMillin, B.K. and Hanson, R.K. (1993) "Temperature Measurements in Gases by Use of Planar Laser-Induced Fluorescence Imaging of NO," *Appl. Optics*, Vol. 32, pp. 5379-5396.

McDermid, I.S. and Laudenslager, J.B. (1982) "Radiative Lifetimes and Electronic Quenching Rate Constants for Single-Photon Excited Rotational Levels of NO ($A^2\Sigma^+$, $\nu' = 0$)," *J. Quant. Spect. Radiat. Transfer*, Vol. 27, pp. 483-492.

Morkovin, M.V. (1961) "Effects of Compressibility on Turbulent Flows," *Mechanique de la Turbulence*, A. Farve ed., pp. 367-380.

Naughton, J.W, Cattafesta, L.N. III, and Settles, G.S. (1997) "An Experimental Study of Compressible Turbulent Mixing Enhancement in Swirling Jets," *J. Fluid Mech.*, Vol. 330, pp. 271-305

Papamoschou, D. and Roshko, A. (1988) "The Compressible Turbulent Shear Layer: An Experimental Study," *J. Fluid Mech.*, Vol. 197, pp. 453-477.

Rossmann, T, Mungal, M.G., and Hanson, R.K. (1999) "A New Shock Tunnel Driven Facility for High Compressibility Mixing Layer Studies," *AIAA 99-0415*, 37th Aerospace Sciences Meeting, Reno, NV.

Rossmann, T., Mungal, M. G., and Hanson, R. K (2002) "Evolution and Growth of Large Scale Structures in High Compressibility Mixing Layers," *J. of Turbulence*, Vol. 3, No. 9, pp. 1-18.

Samimy, M. and Elliot, G.S. (1990) "Effects of Compressibility on the Characteristics of Free Shear Flows," *AIAA Journal*, Vol. 28, pp. 439-445.